

# Phase transitions in fluctuations and their role in two-step nucleation

Cite as: J. Chem. Phys. **150**, 074501 (2019); <https://doi.org/10.1063/1.5057429>

Submitted: 14 September 2018 . Accepted: 16 January 2019 . Published Online: 20 February 2019

Daniella James, Seamus Beairsto , Carmen Hartt, Oleksandr Zavalov , Ivan Saika-Voivod ,  
Richard K. Bowles , and Peter H. Poole 

## COLLECTIONS

 This paper was selected as an Editor's Pick



[View Online](#)



[Export Citation](#)



[CrossMark](#)

# Phase transitions in fluctuations and their role in two-step nucleation

Cite as: J. Chem. Phys. 150, 074501 (2019); doi: 10.1063/1.5057429

Submitted: 14 September 2018 • Accepted: 16 January 2019 •

Published Online: 20 February 2019



View Online



Export Citation



CrossMark

Daniella James,<sup>1</sup> Seamus Beairisto,<sup>1</sup>  Carmen Hartt,<sup>1</sup> Oleksandr Zavalov,<sup>1</sup>  Ivan Saika-Voivod,<sup>2</sup>   
Richard K. Bowles,<sup>3</sup>  and Peter H. Poole<sup>1</sup> 

## AFFILIATIONS

<sup>1</sup>Department of Physics, St. Francis Xavier University, Antigonish, Nova Scotia B2G 2W5, Canada

<sup>2</sup>Department of Physics and Physical Oceanography, Memorial University of Newfoundland, St. John's, Newfoundland A1B 3X7, Canada

<sup>3</sup>Department of Chemistry, University of Saskatchewan, Saskatoon, Saskatchewan S7N 5C9, Canada

## ABSTRACT

We consider the thermodynamic behavior of local fluctuations occurring in a stable or metastable bulk phase. For a system with three or more phases, we present a simple analysis based on classical nucleation theory that predicts thermodynamic conditions at which small fluctuations resemble the phase having the lowest surface tension with the surrounding bulk phase, even if this phase does not have a lower chemical potential. We also identify the conditions at which a fluctuation may convert to a different phase as its size increases, referred to here as a “fluctuation phase transition” (FPT). We demonstrate these phenomena in simulations of a two dimensional lattice model by evaluating the free energy surface that describes the thermodynamic properties of a fluctuation as a function of its size and phase composition. We show that a FPT can occur in the fluctuations of either a stable or metastable bulk phase and that the transition is first-order. We also find that the FPT is bracketed by well-defined spinodals, which place limits on the size of fluctuations of distinct phases. Furthermore, when the FPT occurs in a metastable bulk phase, we show that the superposition of the FPT on the nucleation process results in two-step nucleation (TSN). We identify distinct regimes of TSN based on the nucleation pathway in the free energy surface and correlate these regimes to the phase diagram of the bulk system. Our results clarify the origin of TSN and elucidate a wide variety of phenomena associated with TSN, including the Ostwald step rule.

Published under license by AIP Publishing. <https://doi.org/10.1063/1.5057429>

## I. INTRODUCTION

Fluctuations play a central role in many liquid state phenomena. For example, it has long been appreciated that fluctuations dominate the physics of critical phenomena and second-order phase transitions.<sup>1</sup> Similarly, in the study of supercooled liquids and the origin of the glass transition, local fluctuations that deviate from the average properties of the bulk liquid phase (e.g., dynamical heterogeneities and locally favored structures) continue to be the focus of much work to explain the complex dynamics observed as a liquid transforms to an amorphous solid.<sup>2-4</sup> For network-forming liquids such as water, “two-state” models that assume the occurrence of two distinct, transient local structures have been proposed to explain thermodynamic and dynamic anomalies

occurring in both the stable and supercooled liquids.<sup>5</sup> The central role of fluctuations is perhaps most obvious in nucleation phenomena, where a bulk metastable phase decays to a stable phase via the formation of a local fluctuation (the critical nucleus) of sufficient size to be able to grow spontaneously to a macroscopic scale.<sup>6,7</sup>

The behavior of local fluctuations is particularly complex in the case of “two-step nucleation” (TSN).<sup>8-41</sup> In TSN, the first step in the phase transformation process consists of the appearance in the bulk metastable phase of a local fluctuation that resembles an intermediate phase distinct from the stable phase. In the second step of TSN, this intermediate fluctuation undergoes a transition in which the stable phase emerges from within the intermediate phase. Evidence for TSN has been observed experimentally in a wide range of

molecular and colloidal systems,<sup>10,18,28,34</sup> including important cases relevant to understanding protein crystallization<sup>39,40</sup> and biomineralization.<sup>15,16</sup> Due to the involvement of an intermediate phase, TSN is poorly described by classical nucleation theory (CNT), in which it is assumed that a nucleus of the stable phase appears directly from the metastable phase.<sup>6,7</sup> Large deviations from CNT predictions are thus associated with TSN.<sup>23</sup> Given these challenges, an understanding of TSN is required to better control and exploit complex nucleation phenomena. For example, significant questions remain concerning the nature of long-lived “pre-nucleation clusters” that have been reported in some TSN processes.<sup>15,16,22,27</sup> Control of polymorph selection during nucleation and the origins of the Ostwald step rule (OSR)<sup>7</sup> are also facilitated by a better understanding of TSN.<sup>26,41,42</sup>

A number of theoretical and simulation studies have investigated TSN.<sup>8,9,11–14,17,19–21,24–26,29,31–33,36,37,41</sup> These studies highlight the role of metastable phase transitions involving competing bulk phases and their connection to the transition from the intermediate to the stable fluctuation that occurs in TSN. In addition, several studies have examined TSN in terms of the two dimensional (2D) free energy surface (FES) that quantifies the nucleation pathway as a function of the size of the nucleus and its degree of similarity to the stable phase.<sup>8,17,19–21,29,31,32</sup> For example, Duff and Peters demonstrated the existence of two distinct regimes of TSN, in which the transition of the nucleus to the stable phase occurs either before or after the formation of the critical nucleus, located at the saddle point of the FES.<sup>17</sup> Iwamatsu further showed that the FES for TSN may contain two distinct nucleation pathways, each with its own saddle point.<sup>21</sup> These studies illustrate the complexity of TSN and help us to explain the non-classical phenomena attributed to TSN in experiments.

Despite the insights obtained to date from experiments, theory, and simulation, our understanding of TSN would benefit from a clearer understanding of the relationship between a bulk phase transition and the transition that occurs in the growing nucleus from the intermediate to the stable phase. This latter transition occurs in a finite-sized system (the fluctuation) and is controlled not only by the chemical potential difference between the intermediate and stable phases but also by strong surface effects at the interface with the surrounding bulk metastable phase. In the following, we refer to the transition that occurs in a finite-sized fluctuation as a “fluctuation phase transition” (FPT) to distinguish it from a bulk phase transition, for which surface effects play no role in determining the thermodynamic conditions of the equilibrium transition. It would be particularly useful to know how to predict the conditions at which a FPT will occur and how these conditions are related to the thermodynamic conditions at which bulk phase transitions, both stable and metastable, occur in the same system.

This paper has two aims: First, we seek to clarify the general thermodynamic behavior of local fluctuations, regardless of whether these fluctuations are involved in a nucleation process, to better understand the properties of fluctuations in their own right. Second, we wish to specifically elucidate TSN

via a detailed examination of the local fluctuations that appear during TSN and how the behavior of these fluctuations varies over a wide range of thermodynamic conditions.

To achieve these aims, we first present in Sec. II a simple theoretical analysis of fluctuations. This analysis uses the assumptions of classical nucleation theory (CNT) to make some general predictions on the nature of local fluctuations in either a stable or a metastable phase when more than one type of fluctuation is possible. This analysis identifies a number of distinct thermodynamic scenarios for how fluctuations behave as a function of their size, including predicting the conditions at which a FPT will occur.

In Secs. III–VI, we then describe simulations of a 2D lattice model, which provides a case study in which our analytical predictions can be tested. In particular, the model is simple enough to provide a complete thermodynamic description of the fluctuations, in the form of a FES which characterizes the fluctuations in terms of their size and phase composition. We locate and characterize the FPT as it is observed in the features of the FES for both a stable and metastable phase. Our lattice model results demonstrate that TSN occurs when a FPT is superimposed on a nucleation process occurring in a metastable phase. We are thus able to provide a comprehensive perspective on the origins of TSN, clarify its relationship to bulk phase behavior, and elucidate the non-classical nature of TSN.

In Sec. VII, we discuss the connections between our results and previous studies on TSN, such as Refs. 17 and 21. Our results reproduce a number of observations made previously in separate studies, as well as identifying new behavior that underlies these previous observations, thus unifying our understanding of the origins of TSN and related phenomena. At the same time, our results demonstrate that complex thermodynamic behavior is an intrinsic property of fluctuations, independent of metastability and nucleation. As discussed in Sec. VIII, our findings thus have wider implications for understanding liquid state phenomena that are dominated by the behavior of fluctuations.

## II. CNT ANALYSIS OF FLUCTUATIONS

We begin with an idealized analysis of the fluctuations in a bulk phase when there are two other bulk phases that may occur in the system. As we will see, this analysis suggests the existence of several distinct regimes of fluctuation behavior depending on the thermodynamic conditions, including regimes in which a FPT occurs. Since some of these regimes also correspond to TSN processes, this analysis provides an idealized framework for understanding the origins of TSN. Furthermore, the analysis predicts a regime in which a FPT occurs in a stable phase where nucleation is not possible, demonstrating that a FPT and nucleation can be regarded as independent phenomena.

Consider the free energy cost  $G$  to create a fluctuation of size  $n$  molecules within a bulk phase  $\mathcal{A}$ . We assume that any such fluctuation can be associated with one of two other bulk phases  $\mathcal{B}$  or  $\mathcal{C}$  and that the temperature of the system is such that any bulk transition between phases is first order. We also

assume that the free energy cost to create a fluctuation of  $\mathcal{B}$  or  $\mathcal{C}$  within  $\mathcal{A}$  is given respectively by the CNT expressions,

$$\begin{aligned} G_{AB} &= n^\alpha \phi \sigma_{AB} + n \Delta\mu_{AB}, \\ G_{AC} &= n^\alpha \phi \sigma_{AC} + n \Delta\mu_{AC}, \end{aligned} \quad (1)$$

where  $\sigma_{AB}$  is the  $AB$  surface tension and  $\Delta\mu_{AB} = \mu_B - \mu_A$  is the difference in the chemical potential between the bulk phases  $\mathcal{B}$  and  $\mathcal{A}$  and where  $\sigma_{AC}$  and  $\Delta\mu_{AC}$  are similarly defined.<sup>6,7</sup> Here we assume that the surface area of the fluctuation is  $n^\alpha \phi$ , where  $\alpha = (D - 1)/D$  depends on the dimension of space  $D$  and  $\phi$  is a shape factor. For circular fluctuations in  $D = 2$ ,  $\alpha = 1/2$  and  $\phi = (4\pi v)^{1/2}$ , where  $v$  is the area per molecule. For spherical fluctuations in  $D = 3$ ,  $\alpha = 2/3$  and  $\phi = (36\pi v^2)^{1/3}$ , where  $v$  is the volume per molecule.

Let us now assume that the  $\mathcal{B}$  phase has a lower surface tension with  $\mathcal{A}$  than does  $\mathcal{C}$ , i.e.,  $\sigma_{AB} < \sigma_{AC}$ . Six distinct cases are then possible for the relative behavior of  $G_{AB}$  and  $G_{AC}$ , corresponding to the six possible orderings of the chemical potentials  $\mu_A$ ,  $\mu_B$ , and  $\mu_C$ , as illustrated in Fig. 1. When the  $\mathcal{B}$  phase is more stable than  $\mathcal{C}$  [i.e.,  $\Delta\mu_{CB} = \mu_B - \mu_C < 0$ , corresponding to panels (a)–(c) in Fig. 1], then  $G_{AB}$  is always lower than  $G_{AC}$ , and so the most probable fluctuations of  $\mathcal{A}$  remain  $\mathcal{B}$ -like for all  $n$ . However, when the  $\mathcal{C}$  phase is more stable than  $\mathcal{B}$  [i.e.,  $\Delta\mu_{CB} > 0$ , corresponding to panels (d)–(f) in Fig. 1],  $G_{AB}$

and  $G_{AC}$  will cross at a value of  $n = n_c$  given by

$$n_c^{1/D} = \phi \frac{\sigma_{AC} - \sigma_{AB}}{\Delta\mu_{CB}}. \quad (2)$$

If  $n_c > 1$ , the minimum size of an observable fluctuation, this crossing will manifest itself as a FPT. That is, the fluctuation will resemble the  $\mathcal{B}$  phase when it first appears and then undergoes a transition to the  $\mathcal{C}$  phase as it grows.

Notably, in every panel of Fig. 1, the initial fluctuation is  $\mathcal{B}$ -like. That is, the most probable small fluctuation observed in phase  $\mathcal{A}$  corresponds to the phase that has the lower surface tension with  $\mathcal{A}$ , for any ordering of the chemical potentials  $\mu_A$ ,  $\mu_B$ , and  $\mu_C$ . This statement is always true when  $\Delta\mu_{CB} < 0$  and is true for  $\Delta\mu_{CB} > 0$  when  $n_c > 1$ . When  $\sigma_{AB} < \sigma_{AC}$ , these conditions are equivalent to the condition,

$$\Delta\mu_{CB} < \phi(\sigma_{AC} - \sigma_{AB}), \quad (3)$$

which is satisfied over a wide range of thermodynamic states in a three-phase system. Equation (3) is always satisfied when  $\mathcal{B}$  is more stable than  $\mathcal{C}$  (i.e.,  $\Delta\mu_{CB} < 0$ ), where  $G_{AB} < G_{AC}$  for all  $n$  and  $n_c$  is undefined. In the region of the phase diagram where  $\mathcal{C}$  is more stable than  $\mathcal{B}$  (i.e.,  $\Delta\mu_{CB} > 0$ ), Eq. (3) is satisfied in a band of states delimited by two boundaries. The first boundary corresponds to the  $\mathcal{BC}$  coexistence line, where  $\Delta\mu_{CB} = 0$  and  $n_c$  diverges. The second boundary is given by  $\Delta\mu_{CB} = \phi(\sigma_{AC} - \sigma_{AB})$ , beyond which  $n_c < 1$ . Between these two boundaries, the FPT will occur at an observable and well-defined value of  $n_c > 1$ . Equation (3) is thus satisfied in a region on both sides of the  $\mathcal{BC}$  coexistence line. This region necessarily encompasses the triple point of a three phase system, where complex nucleation phenomena, such as TSN, are commonly observed.

Our analysis thus predicts that whenever Eq. (3) is satisfied (e.g., near a triple point) the initial fluctuations of a bulk phase favor the local structure that has the lowest surface tension, regardless of whether or not other structures have a lower bulk chemical potential. In addition, our analysis does not depend on the value of  $\mu_A$  and thus applies to the behavior of the fluctuations of  $\mathcal{A}$  regardless of whether  $\mathcal{A}$  is stable or metastable with respect to either or both of the bulk  $\mathcal{B}$  and  $\mathcal{C}$  phases. Thus in Fig. 1(e) a FPT occurs in the fluctuations of the stable  $\mathcal{A}$  phase, while in Figs. 1(d) and 1(f), a FPT occurs in the fluctuations of the metastable  $\mathcal{A}$  phase. In these two latter cases, a nucleation process from  $\mathcal{A}$  to  $\mathcal{C}$  occurs in concert with a FPT from  $\mathcal{B}$  to  $\mathcal{C}$ . The cases in Figs. 1(d) and 1(f) may thus be expected to correspond to TSN.

### III. LATTICE MODEL SIMULATIONS

Next we present results obtained from a lattice model to test and elaborate on the predictions of Sec. II. As shown below, this model provides a simple example of a system having a triple point at which three distinct bulk phases coexist. Furthermore, within any one phase, fluctuations corresponding to the other two phases are easily identified.

We conduct Monte Carlo (MC) simulations of a 2D Ising model, with nearest-neighbor (nn) and next-nearest-neighbor (nnn) interactions, on a square lattice of  $N = L^2$  sites with

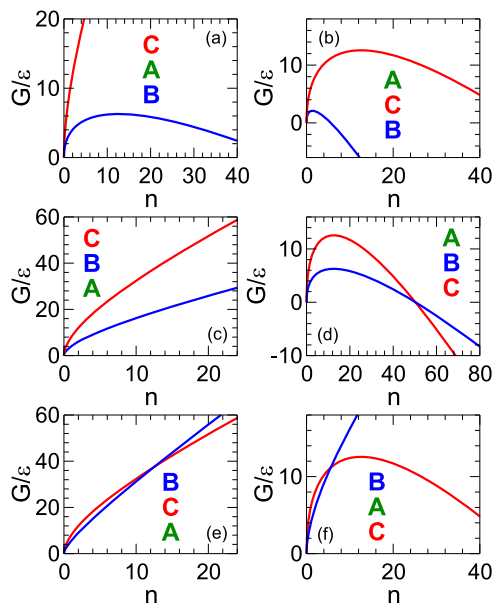


**FIG. 1:**  $G_{AB}$  (blue) and  $G_{AC}$  (red) versus  $n$  for  $D = 2$  in various thermodynamic regimes. To plot these curves, we scale energies by  $\varepsilon = |\Delta\mu_{AC}|$  and surface tensions by  $\varepsilon v^{-\alpha}$ . In all panels,  $\sigma_{AC} = 2\sigma_{AB} = 2\varepsilon v^{-\alpha}$ . In the left-hand side panels,  $\Delta\mu_{AC} = \varepsilon$ , and in the right-hand side panels  $\Delta\mu_{AC} = -\varepsilon$ . From top to bottom within each column,  $\Delta\mu_{AB}$  increases: (a)  $\Delta\mu_{AB} = -\varepsilon/2$ , (b)  $\Delta\mu_{AB} = -3\varepsilon/2$ , (c)  $\Delta\mu_{AB} = \varepsilon/2$ , (d)  $\Delta\mu_{AB} = -\varepsilon/2$ , (e)  $\Delta\mu_{AB} = 2\varepsilon$ , (f)  $\Delta\mu_{AB} = \varepsilon/2$ . To indicate the relative stability of the three bulk phases in each panel, the phases are listed vertically according to their value of  $\mu$ , with  $\mu$  increasing from bottom to top in each list.

periodic boundary conditions. Each site  $i$  is assigned an Ising spin  $s_i = \pm 1$ . The energy  $E$  of a microstate is given by

$$\frac{E}{J} = \sum_{\langle nn \rangle} s_i s_j - \frac{1}{2} \sum_{\langle nnn \rangle} s_i s_j - H \sum_{i=1}^N s_i - H_s \sum_{i=1}^N \sigma_i s_i, \quad (4)$$

where  $J$  is the magnitude of the  $nn$  interaction energy. Interactions between  $nn$  sites are antiferromagnetic, while  $nnn$  interactions are ferromagnetic. The first (second) sum in Eq. (4) is carried out over all distinct  $nn$  ( $nnn$ ) pairs of sites  $i$  and  $j$ . The third and fourth terms in Eq. (4) specify the influence of the direct magnetic field  $H$  and the staggered field  $H_s$ . We define  $\sigma_i = (-1)^{x_i+y_i}$ , where  $x_i$  and  $y_i$  are integer horizontal and vertical coordinates of site  $i$  so that the sign of  $H_s \sigma_i$  alternates in a checkerboard fashion on the lattice. We sample configurations using Metropolis single-spin-flip MC dynamics.<sup>43</sup>

This model has been studied previously to model metamagnetic systems exhibiting a tricritical point, for which it provides a prototypical example in 2D.<sup>44–48</sup> At  $T = 0$ , four stable phases are observed, depending on the values of  $H$  and  $H_s$ . We label these phases so as to maintain the “ $ABC$ ” notation used in Sec. II. There are two ferromagnetic phases which we label  $B$  (all  $s_i = 1$ ) and  $\bar{B}$  (all  $s_i = -1$ ) and two antiferromagnetic phases labelled  $C$  (all  $s_i = \sigma_i$ ) and  $A$  (all  $s_i = -\sigma_i$ ). Since the topology of the phase diagram is unchanged when  $H \rightarrow -H$ , we only consider  $H > 0$  here. Consequently the  $\bar{B}$  phase will not appear in our analysis. All our simulations are carried out at temperature  $T$  such that  $\beta J = 1$ , where  $\beta = 1/kT$  and  $k$  is Boltzmann’s constant. This is well below  $T$  for the Néel transition ( $kT/J = 3.802$ ) and the tricritical point ( $kT/J = 1.205$ ).<sup>46</sup> Thus the phase diagram in the plane of  $H$  and  $H_s$  at fixed  $kT/J = 1$  contains only first-order phase transitions, arranged as three coexistence lines meeting at a triple point located at  $H_s = 0$  and  $H = 3.9876$ , as shown in Fig. 2. See Secs. S1–S3 of the supplementary material and Refs. 43, and 49–51 for the details of our phase diagram calculation.

The phase diagram presented in Fig. 2 also includes the metastable extensions of the  $AC$ ,  $BC$ , and  $AB$  coexistence lines. The phase diagram is thereby divided into six distinct regions each corresponding to a unique ordering of the chemical potentials  $\mu_A$ ,  $\mu_B$ , and  $\mu_C$ . Furthermore, as shown in Sec. S4 of the supplementary material, we find that  $\sigma_{AB} < \sigma_{AC}$  throughout the region of the  $(H_s, H)$  plane explored here.<sup>50,52–54</sup> Our lattice model thus realizes the relationships between the surface tensions and chemical potentials considered in Sec. II: The six regions of the phase diagram in Fig. 2 correspond to the six panels of Fig. 1. If we choose the  $A$  phase of the lattice model to correspond to the  $A$  phase of Sec. II, then the predictions of Sec. II can be tested by examining the behavior of the fluctuations of  $A$  in the lattice model in the various regions of the model phase diagram.

To explore the scenarios predicted in Sec. II, we must characterize the fluctuations that appear in the bulk  $A$  phase. Due to the simplicity of our lattice model, we show in Sec. S5 of the supplementary material that it is straightforward to identify all local fluctuations as clusters of size  $n$  that deviate from the structure of  $A$ . All sites within a given cluster can further

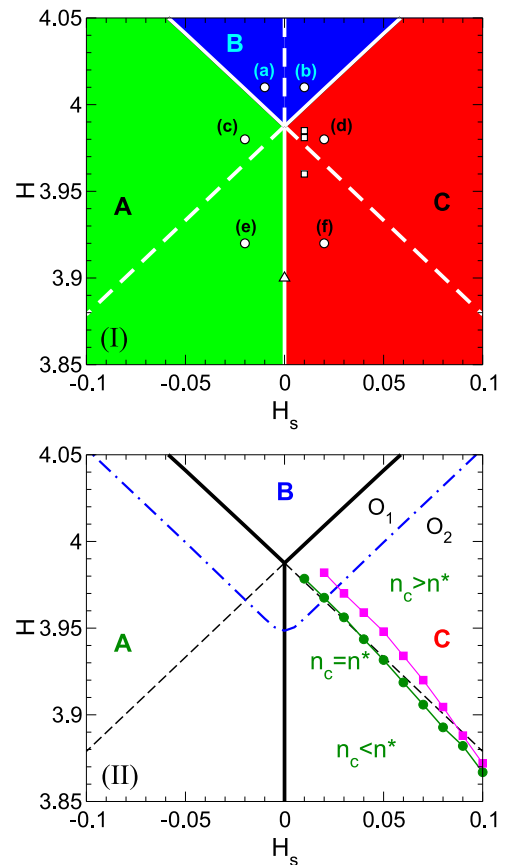


**FIG. 2.** Phase diagram for  $kT/J = 1$ . Solid lines are coexistence lines and dashed lines are metastable extensions of coexistence lines. In panel (I), the stability field of each phase is indicated with a solid color, green for  $A$ , blue for  $B$ , and red for  $C$ . The six regions demarcated by the solid and dashed lines are labelled (a)–(f) and correspond to the six identically labelled cases shown in Fig. 1. The triangle locates the state studied in Sec. IV. Squares locate the three states studied in Sec. V. Circles locate the six states for which the nucleation barriers are presented in Fig. 14. In panel (II), the dotted-dashed line is the limit of metastability (LOM) of the bulk  $B$  phase for a system of size  $L = 64$ . Green circles locate points on the line  $\mathcal{L}_n$  at which  $n_c = n^*$ . Magenta squares locate points on the line at which  $\beta G^* = 20$ ; below this line  $\beta G^* > 20$  and above it,  $\beta G^* < 20$ .  $O_1$  labels the region bounded by the  $AB$  and  $BC$  coexistence lines and the LOM of the  $B$  phase.  $O_2$  labels the region between the  $AB$  and  $BC$  coexistence lines and which lies beyond the LOM of the  $B$  phase.

be classified according to their correspondence to either  $B$  or  $C$ . We thereby define the phase composition of each cluster as  $f = \bar{n}/n$ , where  $\bar{n}$  is the number of sites in the cluster that are classified as  $C$ . Figure 3 shows example clusters of various  $n$  and  $f$ , from mostly  $B$ -like ( $f \rightarrow 0$ ) to mostly  $C$ -like ( $f \rightarrow 1$ ).

To quantify the thermodynamic behavior of the fluctuations that occur in  $A$ , we measure  $G(n_{\max}, f)$ , the FES of the bulk  $A$  phase in which the largest non- $A$  cluster in the system is of size  $n_{\max}$  and has composition  $f$ .<sup>17</sup> We obtain the FES from umbrella sampling MC simulations at fixed  $(N, H_s, H, T)$ .<sup>51</sup> We compute  $G(n_{\max}, f)$  from

$$\beta G(n_{\max}, f) = -\log[P(n_{\max}, f)] + C, \quad (5)$$

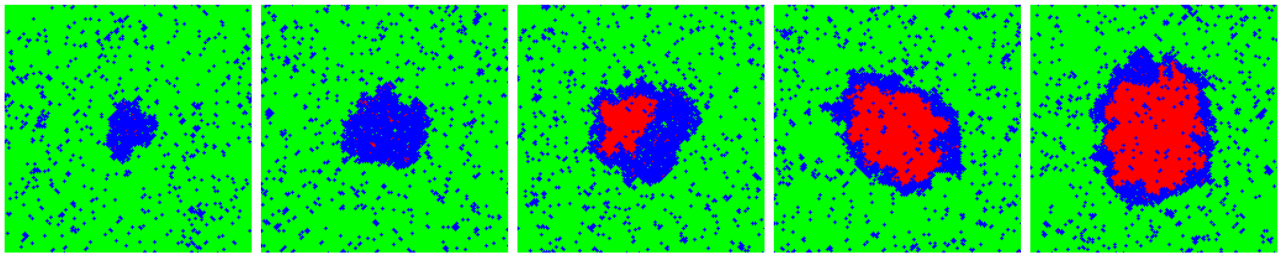


**FIG. 3.** System configurations containing fluctuations of different sizes and compositions obtained from 2D umbrella sampling simulations carried out at  $H_s = 0.01$ ,  $H = 3.981$ , and  $L = 200$ . As described in Sec. S5 of the [supplementary material](#), green sites have a local structure corresponding to the  $\mathcal{A}$  phase, blue to the  $\mathcal{B}$  phase, and red to the  $\mathcal{C}$  phase. From left to right,  $(n_{\max}, f) = (1393, 0.020)$ ,  $(3476, 0.040)$ ,  $(5474, 0.303)$ ,  $(7492, 0.583)$ , and  $(9658, 0.633)$ . This sequence of microstates approximately follows the path of  $\langle f \rangle$  shown in [Fig. 8\(b\)](#) and illustrates the two-step nature of the nucleation process under these conditions.

where  $P(n_{\max}, f)$  is proportional to the probability to observe a microstate with values  $n_{\max}$  and  $f$ . The value of the arbitrary constant  $C$  is chosen so that the global minimum of  $G(n_{\max}, f)$  is zero. We estimate  $P(n_{\max}, f)$  from 2D umbrella sampling simulations using a biasing potential that depends on both  $n_{\max}$  and  $f$ ,

$$U_B = \kappa_n (n_{\max} - n_{\max}^*)^2 + \kappa_f (f - f^*)^2, \quad (6)$$

where  $n_{\max}^*$  and  $f^*$  are the target values of  $n_{\max}$  and  $f$  to be sampled in a given umbrella sampling simulation and  $\kappa_n$  and  $\kappa_f$  control the range of sampling around  $n_{\max}^*$  and  $f^*$ . See Sec. S6 of the [supplementary material](#) for details of our 2D umbrella sampling simulations. Results from multiple umbrella sampling runs conducted at fixed  $(N, H_s, H, T)$  are combined using the weighted histogram analysis method (WHAM) to estimate the full  $G(n_{\max}, f)$  FES at a given state point.<sup>51,55,56</sup> Once  $G(n_{\max}, f)$  has been calculated, we can also compute the one dimensional (1D) free energy as a function of  $n_{\max}$  alone, defined as

$$\beta G_1(n_{\max}) = -\log \int_0^1 \exp[-\beta G(n_{\max}, f)] df. \quad (7)$$

In addition to the 2D umbrella sampling simulations described above, we also conduct 1D umbrella sampling simulations in which  $n_{\max}$  alone is constrained. In this approach, we directly compute  $G_1(n_{\max})$  using

$$\beta G_1(n_{\max}) = -\log[P_1(n_{\max})] + C, \quad (8)$$

where  $P_1(n_{\max})$  is proportional to the probability to observe a microstate with a given value of  $n_{\max}$  and  $C$  is chosen so that the global minimum of  $G_1(n_{\max})$  is zero. The details of our 1D umbrella sampling runs are given in Sec. S7 of the [supplementary material](#). We obtain the size of the critical nucleus  $n^*$  from the value of  $n_{\max}$  at the maximum of  $G_1(n_{\max})$ .

Although the maximum in  $G_1(n_{\max})$  properly identifies  $n^*$ , it is important to note that the height of the maximum in  $G_1(n_{\max})$  does not correspond to the nucleation barrier described by CNT. The nucleation barrier is more accurately estimated by computing,

$$\beta \bar{G}(n) = -\log \frac{\mathcal{N}(n)}{N}, \quad (9)$$

where  $\mathcal{N}(n)$  is the average number of clusters of size  $n$  in a system of size  $N$ .<sup>57-59</sup> The height of the nucleation barrier is then defined as  $G^* = \bar{G}(n^*)$ . Since we also evaluate  $\mathcal{N}(n)$  from our 1D umbrella sampling simulations, we are able to estimate  $\bar{G}(n)$  and  $G^*$  for these cases. Examples of our calculations of  $\bar{G}(n)$  are given in Sec. S8 of the [supplementary material](#).

#### IV. FLUCTUATION PHASE TRANSITION IN A STABLE PHASE

In this section, we analyze the behavior observed in the fluctuations of  $\mathcal{A}$  when  $\mathcal{A}$  is stable and no nucleation process is possible. As an example, we focus on the state point  $(H_s, H) = (0, 3.9)$ . This point is on the  $\mathcal{AC}$  coexistence line, and so the nucleation barrier to convert  $\mathcal{A}$  to  $\mathcal{C}$  is infinitely large. In terms of the analysis of Sec. II, this point is on the boundary of the regions described by panels (e) and (f) of [Fig. 1](#). We thus expect that the fluctuations of  $\mathcal{A}$  are  $\mathcal{B}$ -like at small  $n_{\max}$  and then undergo a FPT to  $\mathcal{C}$  at  $n_c$ .

We present the FES describing the fluctuations of  $\mathcal{A}$  at this state point in [Fig. 4](#). Under these conditions, all local fluctuations that induce a deviation from the most probable state of the  $\mathcal{A}$  phase increase the system free energy, regardless of their size or composition. The FES therefore exhibits only one basin with a minimum in the lower-left corner of [Fig. 4\(b\)](#) associated with the bulk  $\mathcal{A}$  phase, and no transition states (i.e., saddle points) occur on the surface. However, the FES is not featureless. It contains two channels, indicated by the red and blue lines in [Fig. 4\(b\)](#). These lines locate the values of  $f$  at which a local minimum occurs in  $G(n_{\max}, f)$  at a fixed value of  $n_{\max}$ . Along the low- $f$  channel,  $\mathcal{B}$  fluctuations dominate, while the high- $f$  channel corresponds to fluctuations in which the core is  $\mathcal{C}$ , wetted by a surface layer of  $\mathcal{B}$ . We define  $f_B$  as the values of  $f$  along the minimum of the low- $f$  channel and  $f_C$  for the high- $f$  channel.

It is notable that the two channels are unconnected and that neither channel is defined for all  $n_{\max}$ . At small  $n_{\max}$ , only the  $\mathcal{B}$  channel exists, while only the  $\mathcal{C}$  channel exists at large  $n_{\max}$ . This behavior is highlighted in [Fig. 5](#), where we show cuts through the FES at fixed  $n_{\max}$ . For a finite range of  $n_{\max}$ ,  $G$  versus  $f$  exhibits two minima with a maximum in between. At

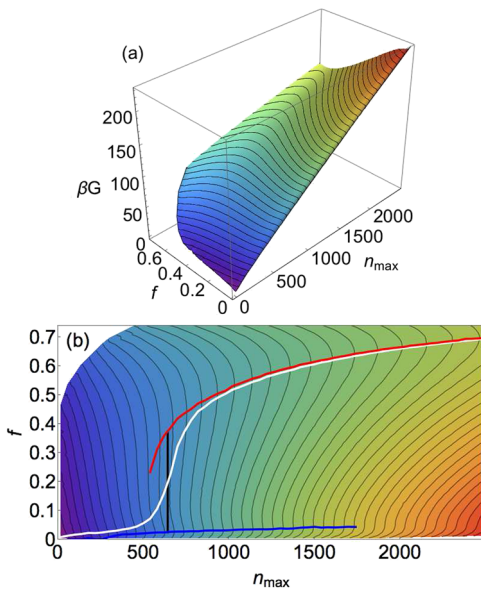


**FIG. 4.** (a) Surface plot and (b) contour plot of  $G(n_{\max}, f)$  for  $(H_s, H) = (0, 3.9)$  and  $L = 128$ . Contours are  $5kT$  apart in both (a) and (b). In (b), we also plot  $f_B$  (blue line),  $f_C$  (red line), and  $f$  (white line). The black vertical line is located at  $n_{\max} = n_c$ .

small  $n_{\max}$ , the high- $f$  minimum disappears, and at large  $n_{\max}$ , the low- $f$  minimum disappears.

To quantify the relative free energies associated with these two channels, we define, for a fixed value of  $n_{\max}$ ,

$$\begin{aligned} \beta G_B &= -\log \int_0^{f_{\max}} \exp[-\beta G(n_{\max}, f)] df, \\ \beta G_C &= -\log \int_{f_{\max}}^1 \exp[-\beta G(n_{\max}, f)] df, \end{aligned} \quad (10)$$

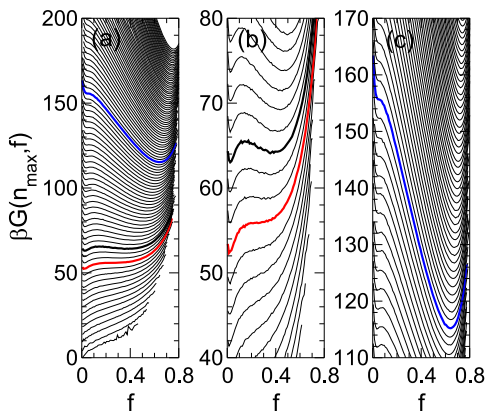


**FIG. 5.** Cuts through the  $G(n_{\max}, f)$  surface at fixed  $n_{\max}$  for  $(H_s, H) = (0, 3.9)$  and  $L = 128$ .  $n_{\max}$  changes by 40 from one cut to the next. Several cuts are highlighted: The red curve is for  $n_{\max} = 539$  and corresponds to the spinodal endpoint of the  $C$  channel. The blue curve is for  $n_{\max} = 1739$  and corresponds to the spinodal endpoint of the  $B$  channel. The thick black curve is for  $n_{\max} = 659$  and corresponds to the point of coexistence between the  $B$  and  $C$  channels at  $n_{\max} = n_c$ .

where  $f_{\max}$  is the value of  $f$  at which a local maximum occurs in  $G(n_{\max}, f)$  as a function of  $f$  at fixed  $n_{\max}$  if the maximum exists. If  $f_B$  is defined but  $f_C$  is not, then  $f_{\max}$  is set to 1. If  $f_C$  is defined but  $f_B$  is not, then  $f_{\max}$  is set to 0. So defined  $G_B$  and  $G_C$  decompose  $G_1$  into contributions associated with the respective  $B$  and  $C$  channels.

We plot  $G_B$ ,  $G_C$ , and  $G_1$  in Fig. 6. We see that the  $B$  channel makes the dominant contribution to the total free energy at small  $n_{\max}$ , while the  $C$  channel dominates at large  $n_{\max}$ . A well-defined FPT is identified by the intersection of  $G_B$  and  $G_C$  and corresponds to a “kink” in the  $G_1$  curve. The value of  $n_{\max}$  at this intersection defines  $n_c$  and identifies the coexistence condition where distinct  $B$ -dominated and  $C$ -dominated fluctuations of equal size are equally probable. We further see that both the channels have metastable extensions beyond  $n_c$  that end at well-defined limits of metastability (LOM), occurring at the values of  $n_{\max}$  where the low- $f$  and high- $f$  minima disappear, as highlighted in Fig. 5. In the following, we use the term “spinodal” to refer to the limit of metastability that terminates a channel in the FES, in analogy to the use of this term when referring to the limit of metastability of a bulk phase in a mean-field system. The behavior shown in Fig. 6, where both coexistence and metastability are observed, demonstrates that the FPT is a first-order phase transition occurring in a finite-sized system (the fluctuation) as the system size ( $n_{\max}$ ) increases.

An appropriate order parameter for the FPT is  $f$ . For a fixed value of  $n_{\max}$ , we define

$$\langle f \rangle = \frac{\int_0^1 f \exp[-\beta G(n_{\max}, f)] df}{\int_0^1 \exp[-\beta G(n_{\max}, f)] df}. \quad (11)$$

We plot  $\langle f \rangle$  in Fig. 4(a). The variation of  $\langle f \rangle$  is steepest at  $n_{\max} = n_c$ . Even though the FPT is first-order,  $\langle f \rangle$  does not jump discontinuously at  $n_c$  because of the finite size of the system. However, the most probable value of  $f$  does have a jump discontinuity at  $n_c$ . We also note that the fluctuations of  $f$  at fixed

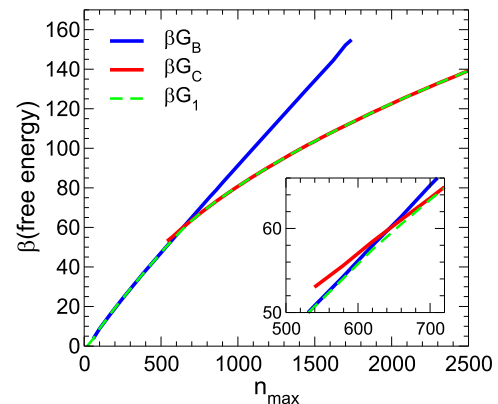


**FIG. 6.**  $G_B$ ,  $G_C$ , and  $G_1$  for  $(H_s, H) = (0, 3.9)$  and  $L = 128$ . The inset shows a closeup of the same data as in the main panel highlighting the intersection of  $G_B$  and  $G_C$  at  $n_{\max} = n_c$ .

$n_{\max}$  can be defined as

$$\chi = \langle f^2 \rangle - \langle f \rangle^2. \quad (12)$$

As shown in Sec. S9 of the [supplementary material](#),  $n_c$  can be accurately estimated as the value of  $n_{\max}$  at which a maximum occurs in  $\chi$ . This procedure allows  $n_c$  to be evaluated without having to separately compute  $G_B$  and  $G_C$ .

The spinodal endpoints that terminate the  $G_B$  and  $G_C$  curves are a significant difference between the behavior plotted in [Fig. 6](#) and that predicted in [Fig. 1\(e\)](#). In our lattice model, a thermodynamic distinction between the  $B$  and  $C$  fluctuations only exists for  $n_{\max}$  between these spinodals, where both channels are observed. These spinodals have important physical consequences. At small  $n_{\max}$ , the most probable fluctuations are always  $B$ -like;  $C$ -like fluctuations, although they may occur, have no local stability relative to changes in  $f$ . This occurs in spite of the fact that  $C$  has a lower bulk-phase chemical potential than  $B$  under these conditions. Thus the prediction made in Sec. II, that the most probable small fluctuation corresponds to the phase with the lowest surface tension, becomes even stronger in our lattice model: Not only is this small fluctuation most probable but also it is the *only* fluctuation that is stable with respect to changes in composition. This observation is in line with a similar conclusion obtained by Harrowell, who predicted that sub-critical clusters in a supercooled liquid are not stable as crystal-like clusters below a threshold size.<sup>60</sup> The same is true here for our  $C$  fluctuations.

Conversely, at sufficiently large  $n_{\max}$ , only  $C$  fluctuations are stable with respect to changes in composition. That is, even though a fluctuation is most likely to start out as a  $B$  fluctuation and even if it persists as a  $B$  fluctuation in the metastable portion of the  $B$  channel when  $n_{\max} > n_c$ , it cannot remain a  $B$  fluctuation at arbitrarily large  $n_{\max}$ . It must eventually convert to  $C$ .

Most of the features of the FES discussed here, including the FPT, occur for  $G \gg kT$ . As a consequence, the most commonly observed fluctuations of  $\mathcal{A}$  are entirely dominated by  $B$ , despite the lower bulk chemical potential of  $C$ . Nonetheless, observable effects associated with the FPT can be observed in this system during non-equilibrium processes. For example, consider the case in which a large cluster of the  $C$  phase is inserted into the bulk  $\mathcal{A}$  phase under the conditions corresponding to the FES in [Fig. 4](#) so that the system starts out close to the  $C$  channel at large  $f$  and large  $n_{\max}$ . If this non-equilibrium system is then allowed to evolve unconstrained, the  $C$  cluster will spontaneously shrink in size and the system point will flow “downhill” along the  $C$  channel of the FES. So long as the degrees of freedom associated with changes in  $f$  relax quickly relative to the rate at which the cluster size decreases, the shrinking cluster will then undergo a FPT from  $C$  to  $B$  at some size between  $n_c$  and the spinodal of the  $C$  channel. The  $B$  cluster so formed will then spontaneously shrink and disappear as the system approaches equilibrium in the lower left-hand corner of the FES. On the other hand, if a large cluster of the  $B$  phase is inserted into the bulk  $\mathcal{A}$  phase under the same conditions so that the system starts out on the  $B$  channel at low  $f$ , the system evolution will follow the

$B$  channel downhill towards equilibrium. In this case, the  $B$  cluster will simply shrink and disappear and no FPT will be observed.

These examples illustrate the differences between the FPT described here and a conventional first-order phase transition occurring between bulk phases. The FPT occurs in a finite-sized system (the fluctuation), which arises as a departure from the most probable state of the surrounding system (the homogeneous bulk phase). In a bulk phase transition, the parameter that drives the system through the phase transition is usually an externally imposed quantity, such as temperature or pressure. However, as in the examples above, the parameter that drives the fluctuation through the FPT is the size of the fluctuation itself. The size of a fluctuation will normally be subject to strong thermodynamic driving forces that cause it to spontaneously increase or decrease in size. The dynamics of the system and its preparation history will therefore have a significant influence on if and how a FPT is observed in a particular case.

## V. TWO-STEP NUCLEATION: FLUCTUATION PHASE TRANSITION IN A METASTABLE PHASE

We now focus on state points where  $\mathcal{A}$  is metastable and  $C$  is stable, i.e., regions (d) and (f) in the phase diagram of [Fig. 2](#). Based on the predictions of Sec. II, we expect in regions (d) and (f) that small  $B$  fluctuations appear first and then convert to  $C$  at larger size via a FPT, just like in region (e). However, in regions (d) and (f), we should also observe a transition state in the FES that is absent in region (e). For  $n_{\max}$  beyond this transition state, the fluctuation will grow in size spontaneously, leading ultimately to the formation of the bulk  $C$  phase. In this case,  $C$  is formed from  $\mathcal{A}$  via a TSN process, in which the  $B$  fluctuations that occur initially play the role of the intermediate phase.

[Figures 7 and 8](#) show the FES at fixed  $H_s = 0.01$  for three values of  $H$  within the stability field of  $C$ .  $G_1$ ,  $G_B$ , and  $G_C$  are shown for each of these cases in [Fig. 9](#). In Sec. S10 of the [supplementary material](#), we provide additional plots of the FES for other values of  $H$  between 3.960 and 3.985. The free energy basin in the lower left corner of each surface in [Fig. 8](#) now corresponds to the metastable bulk  $\mathcal{A}$  phase, and the channel in the upper right corner leads to the stable  $C$  phase. In all cases, we observe a FPT with the same set of features found when  $\mathcal{A}$  is stable: There are two distinct, unconnected channels in the FES. As shown in [Fig. 9](#), the coexistence value of  $n_c$  is well defined at the crossing of  $G_B$  and  $G_C$  and is coincident with a kink in  $G_1$ . The variation of  $\langle f \rangle$  with  $n_{\max}$  is steepest in the vicinity of  $n_c$  ([Fig. 8](#)). We also observe the lower spinodal limit for the  $C$  channel; the upper spinodal limit for the  $B$  channel is beyond the range of  $n_{\max}$  accessible to our simulations for this system size ( $L = 200$ ).

In [Fig. 10](#), we show  $G(n_{\max} = n_c, f)$ , the cut through the  $G(n_{\max}, f)$  surface at the point of coexistence between the  $B$  and  $C$  channels, for each FES plotted in [Figs. 7 and 8](#). We see that the height of the free energy barrier between the two channels at the coexistence condition increases with  $n_c$ . This is in line with the expectation for a first-order phase transition

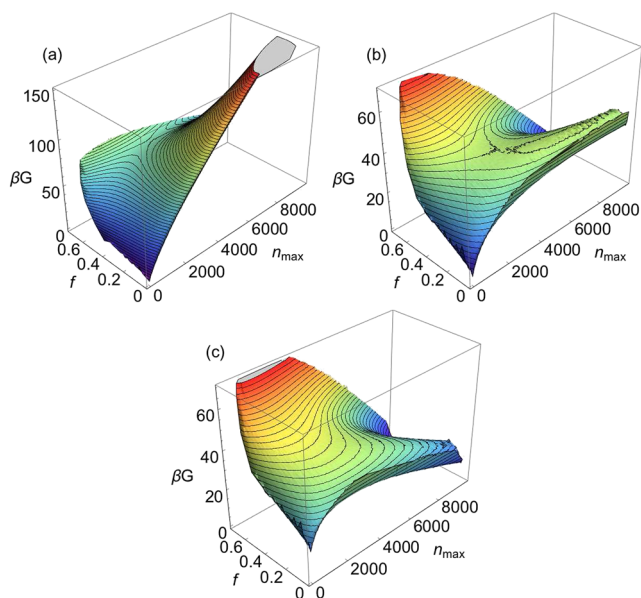


**FIG. 7.** Surface plots of  $G(n_{\max}, f)$  for  $H_s = 0.01$  and  $L = 200$ . Panels (a), (b), and (c) correspond to  $H = \{3.96, 3.981, 3.985\}$ , respectively. Contours are  $2kT$  apart.

occurring in a finite-sized system (i.e., the fluctuation).<sup>52,53</sup> As the size of the fluctuation increases, the phase transition within it must surmount a larger barrier because of the larger interface that must be created between the  $\mathcal{C}$ -like core and the wetting layer of  $\mathcal{B}$  that surrounds the core.

In addition to the FPT, each FES in Figs. 7 and 8 exhibits features associated with the nucleation process by which the metastable  $\mathcal{A}$  phase converts to the stable  $\mathcal{C}$  phase. Figure 9 shows that  $G_1$  in this regime exhibits a maximum at  $n_{\max} = n^*$  corresponding to the size of the critical nucleus. We also observe that the kink in  $G_1$  corresponding to  $n_{\max} = n_c$  may occur either before or after  $n^*$ . Figures 8(a) and 8(c) thus typify two distinct regimes of behavior: In Fig. 8(a),  $n_c < n^*$  while in Fig. 8(c)  $n_c > n^*$ . We also see in Figs. 8(a) and 8(c) that the value of  $n^*$  corresponds closely to  $n_{\max}$  at which a saddle point occurs in the FES. This saddle point locates the most probable transition state at which the system exits the basin of the metastable phase. Thus the FPT can occur either before or after the transition state. We also find that all the qualitative features of the FPT occur in exactly the same way regardless of whether the FPT occurs before or after the transition state. This behavior emphasizes that the FPT is an independent phenomenon from the nucleation process.

Our results thus demonstrate that the superposition of a FPT on the nucleation process generates the characteristic signatures of TSN. When  $n_c < n^*$  [Fig. 8(a)], the FPT occurs in the sub-critical nucleus. In this case, the most probable small nucleus resembles the  $\mathcal{B}$  phase and a small  $\mathcal{C}$  nucleus is unstable with respect to fluctuations in  $f$ . Then as it grows larger the most probable nucleus switches to the  $\mathcal{C}$  phase (via the FPT) prior to reaching the critical size, and so the structure of the

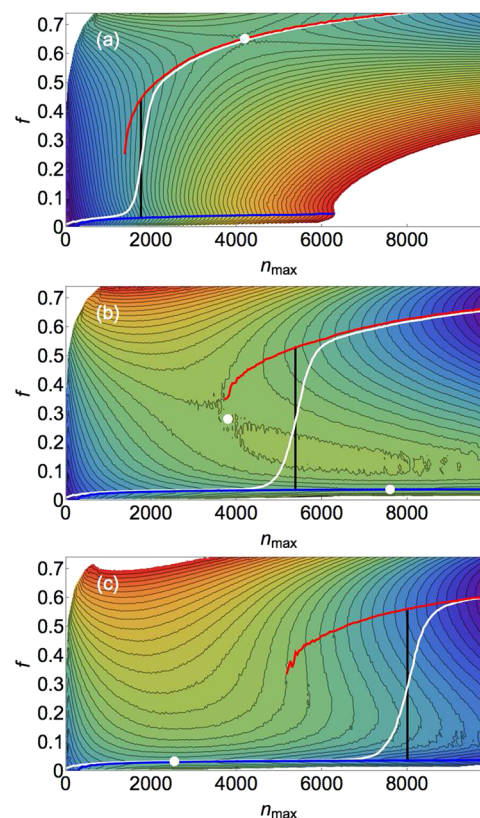


**FIG. 8.** Contour plots of  $G(n_{\max}, f)$  for  $H_s = 0.01$  and  $L = 200$ . Panels (a), (b), and (c) correspond to  $H = \{3.96, 3.981, 3.985\}$ , respectively. Contours are  $2kT$  apart. In each panel, we also plot  $f_B$  (blue line),  $f_C$  (red line), and  $\langle f \rangle$  (white line). The black vertical line is located at  $n_{\max} = n_c$ . The white dots locate saddle points in the FES.

critical nucleus reflects the structure of the bulk stable phase that will ultimately form.

When  $n_c > n^*$  [Fig. 8(c)], the FPT occurs in the post-critical nucleus. In this regime, the most probable nucleus resembles the  $\mathcal{B}$  phase all the way up to and beyond the size of the critical nucleus. Indeed, in Fig. 8(c), we see that a  $\mathcal{C}$  nucleus is unstable at  $n^*$ . As a consequence, the structure of the most probable critical nucleus bears no resemblance to the stable  $\mathcal{C}$  phase, and cannot do so, even as a metastable nucleus. The post-critical  $\mathcal{B}$  nucleus then grows spontaneously along the  $\mathcal{B}$  channel in the FES. The transition of this growing post-critical  $\mathcal{B}$  nucleus to the  $\mathcal{C}$  channel only becomes thermodynamically possible for  $n_{\max}$  greater than that of the lower spinodal for the  $\mathcal{C}$  channel and is only likely to occur for  $n_{\max} \geq n_c$ . These observations emphasize that the transition state (saddle point) is not necessarily the entrance to the basin of the stable phase. Rather, it only identifies the exit from the basin of the metastable phase.

The topology of the FES in Fig. 8(c) exposes the difference between the first and second “steps” of TSN when  $n_c > n^*$ . The first step is a conventional barrier-crossing process where the transition state corresponds to a well-defined

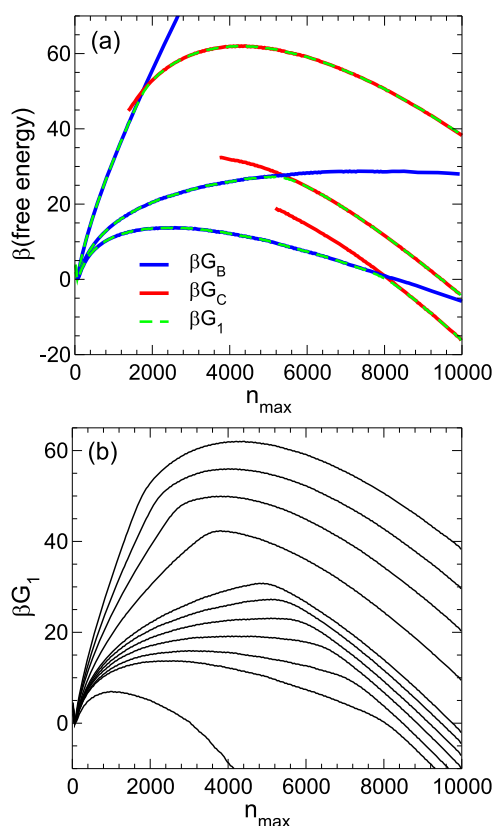


**FIG. 9.** (a)  $G_B$ ,  $G_C$ , and  $G_1$  for  $H_s = 0.01$  and  $L = 200$ . From top to bottom,  $H = \{3.96, 3.981, 3.985\}$ . (b)  $G_1$  for  $H_s = 0.01$  and  $L = 200$ . From top to bottom  $H = \{3.960, 3.965, 3.970, 3.975, 3.980, 3.981, 3.982, 3.983, 3.984, 3.985, 3.990\}$ .

saddle point. The size and composition of the critical nucleus at this step are defined solely by the thermodynamic features encoded in the FES. The second step is associated with the

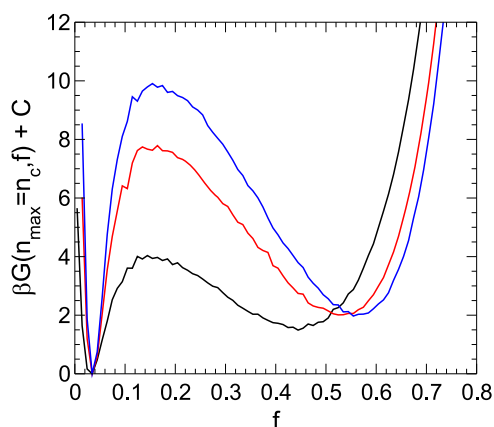


**FIG. 10.**  $G(n_{\text{max}} = n_c, f)$  for  $H_s = 0.01$  and  $L = 200$ . The black curve corresponds to  $H = 3.96$  and  $n_{\text{max}} = 1779$ . The red curve corresponds to  $H = 3.981$  and  $n_{\text{max}} = 5379$ . The blue curve corresponds to  $H = 3.985$  and  $n_{\text{max}} = 8019$ . Each curve has been shifted by a constant  $C$  so that the minimum value is zero.

FPT and is a process where the system does not pass through a saddle point but rather crosses over an extended ridge in the FES.<sup>21</sup> Consequently, even though  $n_c$  is defined by the properties of the FES, the average size of the post-critical nucleus when it crosses the ridge may not be determined solely by the FES. For example, if the degrees of freedom associated with changes in  $f$  relax much faster than those associated with changes in the size of the nucleus, then we can expect the FPT to occur close to  $n_c$ . In this case, the average path of the system on the FES will follow closely the curve for  $\langle f \rangle$ . However, if the relaxation of  $f$  is comparable to or slower than for  $n_{\text{max}}$ , then it is likely that the growing nucleus will significantly “overshoot” the coexistence condition at  $n_c$  and continue to grow in size along the (now metastable)  $\mathcal{B}$  channel. In this case, the average path of the system on the FES will not follow  $\langle f \rangle$ . Thus when  $n_c > n^*$ , the second step of TSN is qualitatively different from the first: The nucleation pathway for the first step is entirely controlled by thermodynamics, whereas the pathway for the second step depends on both thermodynamic and dynamic factors. This distinction can help explain the wide variety of behavior observed in TSN in different systems.

Figure 8(b) corresponds to the case when  $n_c \sim n^*$  and displays complex behavior. We observe two saddle points on either side of an unusually flat region of the FES. Although  $n_c$  and  $n^*$  are close in value,  $n^*$  is not close to the value of  $n_{\text{max}}$  of either saddle point. In this case, the transition state in the FES by which the system leaves the metastable state is not sharply defined. As a consequence, we can expect particularly strong deviations from CNT in this regime.

An example of the unusual behavior occurring when  $n_c \sim n^*$  is shown in Fig. 11, where we plot  $n_c$  and  $n^*$  as a function of  $H$  at fixed  $H_s = 0.01$ . As shown in Fig. 9, the height of the nucleation barrier decreases monotonically as  $H$  increases. However, in Fig. 11, we observe that  $n^*$  does not decrease monotonically with  $H$  but rather exhibits a minimum and a maximum in the vicinity of the value of  $H$  at which  $n_c = n^*$ .

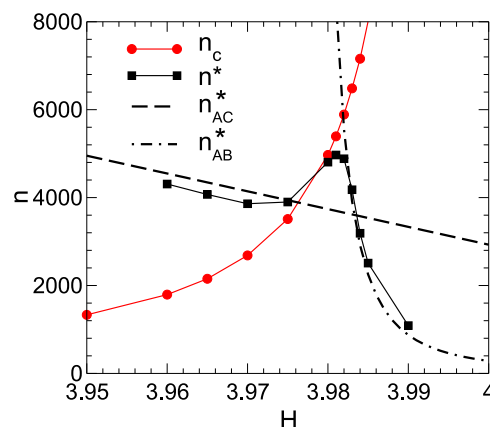


**FIG. 11.** Plot of  $n_c$  and  $n^*$  versus  $H$ , for  $H_s = 0.01$  and  $L = 200$  as obtained from our 2D umbrella sampling simulations. Also shown are the CNT predictions for  $n_{AB}^*$  and  $n_{AC}^*$  computed as described in the text.

This complex and highly non-classical behavior arises from the crossover from the  $n_c < n^*$  to the  $n_c > n^*$  regime as  $H$  increases. To understand this effect, we consider the CNT expression<sup>6,7</sup> for  $n^*$  in  $D = 2$ ,  $n^* = \pi\sigma^2/(\Delta\mu)^2$ . As described in the [supplementary material](#), we have obtained approximate expressions to describe the dependence on  $H$  and  $H_s$  of the chemical potentials (see Sec. S3 of the [supplementary material](#)) and surface tensions (see Sec. S4 of the [supplementary material](#)) for all three phases in our lattice model. We use these expressions to calculate the CNT prediction for the variation of  $n^*$  with  $H$  and compare this with the observed behavior. In [Fig. 11](#), we show that for  $n_c < n^*$ , the  $H$ -dependence of  $n^*$  approximately follows that expected for the nucleation of  $\mathcal{C}$  directly from  $\mathcal{A}$ ,  $n_{AC}^* = \pi\sigma_{AC}^2/(\Delta\mu_{AC})^2$ . While  $\Delta\mu_{AC}$  is constant for all  $H$  at fixed  $H_s$ ,  $n_{AC}^*$  decreases gradually with  $H$  due to the approximately linear decrease of  $\sigma_{AC}^2$  with  $H$ . However, when  $n_c > n^*$ , the  $H$ -dependence of  $n^*$  switches to follow the prediction for the nucleation of  $\mathcal{B}$  directly from  $\mathcal{A}$ ,  $n_{AB}^* = \pi\sigma_{AB}^2/(\Delta\mu_{AB})^2$ . In this expression,  $\sigma_{AB}$  is constant with  $H$ , but the magnitude of  $\Delta\mu_{AB}$  increases linearly as  $H$  increases at fixed  $H_s$ , resulting in a fast decrease of  $n^*$ . The crossover in the behavior of  $n^*$  occurs when the barrier for the  $\mathcal{A} \rightarrow \mathcal{B}$  process becomes smaller than that for the  $\mathcal{A} \rightarrow \mathcal{C}$  process. Interestingly, at the point of this crossover, the critical nucleus along the  $\mathcal{B}$  channel is larger than that on the  $\mathcal{C}$  channel, resulting in the maximum in  $n^*$  observed in [Fig. 11](#).

## VI. TWO-STEP NUCLEATION AND BULK PHASE BEHAVIOR

We next seek to identify where in the phase diagram the different regimes of TSN occur. To do so, we quantify the variation of  $n_c$  and  $n^*$  over a wide range of  $H$  and  $H_s$  within the stability fields of  $\mathcal{A}$  and  $\mathcal{C}$ . We achieve this efficiently by augmenting the results obtained from our 2D umbrella sampling runs with 1D umbrella sampling simulations, as described in Sec. S7 of the [supplementary material](#). As shown in [Fig. 12\(a\)](#), we find that the variation of  $n_c$  with  $H$  and  $H_s$  is relatively simple: For fixed  $H_s$ ,  $n_c$  grows and diverges as  $H$  approaches the  $\mathcal{BC}$  coexistence line  $\mathcal{L}_{BC}$  from below. This behavior is anticipated by the form of Eq. (2) and confirmed in [Fig. 13](#), where we plot  $n_c$  as a function of  $\Delta\mu_{CB}$  for various values of  $H_s$ , both positive and negative. The data for all values of  $H_s$  fall on a single master curve. [Figure 13](#) confirms the prediction of Eq. (2) that  $n_c$  diverges as  $\Delta\mu_{CB} \rightarrow 0$  (i.e., approaching  $\mathcal{L}_{BC}$ ) and does not depend on  $\mu_A$ , which changes as  $H_s$  changes. That is, the value of  $n_c$  is unaffected by the presence or absence of a nucleation process and is an intrinsic property of the fluctuations of  $\mathcal{A}$ .

The variation of  $n^*$  for various  $H_s$  is shown in [Fig. 12\(b\)](#). We find that the maximum of  $n^*$  noted in [Fig. 11](#) is sharpest at small  $H_s$  and fades in prominence as  $H_s$  increases. For each  $H_s$ , we locate the intersection of  $n_c$  and  $n^*$  and plot the locus of points  $\mathcal{L}_n$  at which  $n_c = n^*$  in [Fig. 2](#). For  $H$  less than  $\mathcal{L}_n$ , TSN will be observed where  $n_c < n^*$ ; for  $H$  greater than  $\mathcal{L}_n$ , TSN with  $n_c > n^*$  will occur.

Notably, we find that  $\mathcal{L}_n$  is nearly coincident with the  $\mathcal{AB}$  coexistence line  $\mathcal{L}_{AB}$ , especially as  $H_s \rightarrow 0$ . This

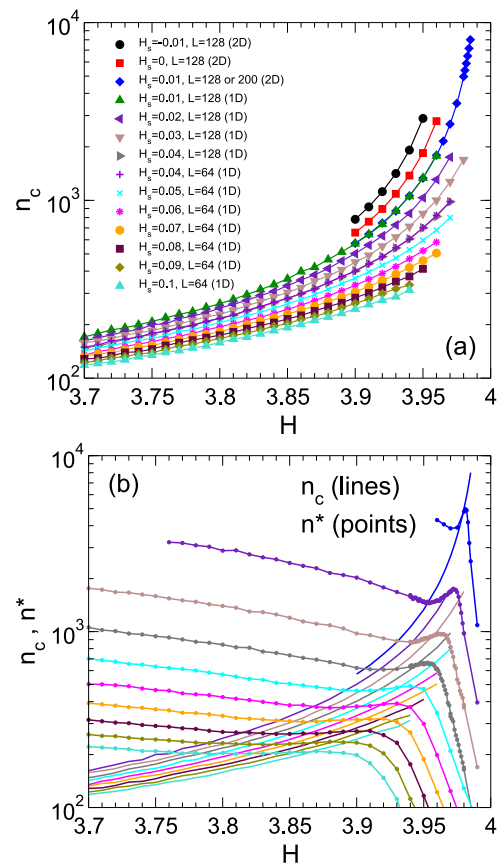


**FIG. 12.** (a)  $n_c$  versus  $H$  for various  $H_s$ . Data are obtained from either 1D or 2D umbrella sampling simulations, as indicated in the legend. For data obtained from 2D umbrella sampling runs at  $H_s = 0.01$ , we use a system of size  $L = 128$  for  $H < 3.96$  and  $L = 200$  for  $H \geq 3.96$ . (b) Lines without symbols plot  $n_c$  versus  $H$ , for  $H_s$  from 0.01 to 0.10 in steps of 0.01, from top to bottom. Lines with dots plot our data for  $n^*$  versus  $H$ , for the same set of  $H_s$  values, from top to bottom. Data for  $n^*$  at  $H_s = 0.01$  are obtained from 2D umbrella sampling runs with  $L = 200$ . Data for  $n^*$  at  $H_s = \{0.02, 0.03, 0.04\}$  are obtained from 1D umbrella sampling runs with  $L = 128$ . All other  $n^*$  data are obtained from 1D umbrella sampling runs with  $L = 64$ .

correspondence occurs in our model due to a combination of influences. Based on Eq. (1), we would expect that  $\mathcal{L}_n$  should occur for  $H$  above  $\mathcal{L}_{AB}$  since  $\Delta\mu_{AB} < 0$  is required to form a  $\mathcal{B}$ -like nucleus that grows spontaneously within  $\mathcal{A}$ . However, [Fig. 11](#) shows that the intersection of  $n_c$  and  $n^*$  occurs at lower  $H$  than predicted by our simple CNT analysis due to the complexity of the FES when  $n_c \sim n^*$ . In addition, we see in [Fig. 12\(b\)](#) that  $n^*$  drops very quickly for  $H$  above  $\mathcal{L}_n$ . Related to this behavior, we also observe that the height of the nucleation barrier  $G^*$  decreases rapidly for  $H$  above  $\mathcal{L}_n$ . See Sec. S8 of the [supplementary material](#) for an example of our calculation of  $G^*$ .<sup>57-59</sup> In [Fig. 2](#), we plot the locus along which  $\beta G^* = 20$ , which we find lies close to and just above  $\mathcal{L}_n$ . For  $H$  above the  $\beta G^* = 20$  locus, the basin of metastability for  $\mathcal{A}$  quickly becomes poorly defined and the TSN process consists of an almost barrierless decay to a spontaneously growing

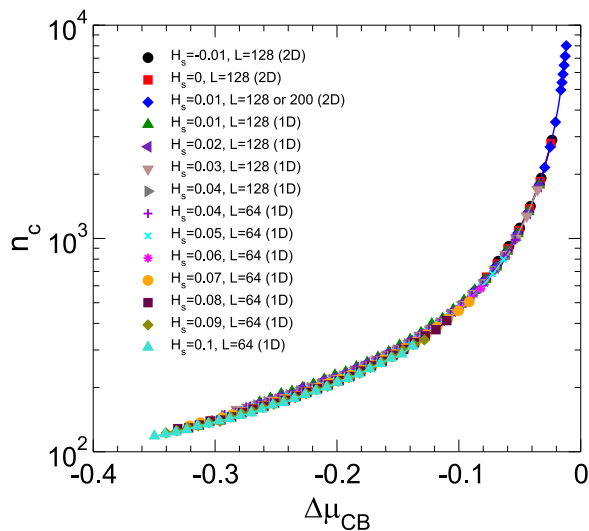


FIG. 13. Same data as in Fig. 12(a) but plotted versus  $\Delta\mu_{CB}$  instead of  $H$ .

nucleus of  $\mathcal{B}$ , which eventually converts to  $\mathcal{C}$  via the FPT. As a result of these effects,  $\mathcal{L}_n$  is on the one hand unlikely to occur much below  $\mathcal{L}_{AB}$  and on the other hand is unlikely to occur much above it. These factors effectively constrain  $\mathcal{L}_n$  to lie very close to  $\mathcal{L}_{AB}$ . If this behavior proves to be common in other systems, it provides a simple way to predict the crossover from the  $n_c < n^*$  to the  $n_c > n^*$  regime, by locating the metastable extension of the bulk phase coexistence line for the two phases involved in the FPT.

We have also assessed the limits of metastability (LOM) of the bulk  $\mathcal{B}$  phase, as described in Sec. S2 of the [supplementary material](#). In practice, the LOM of a homogeneous bulk phase depends on the system size.<sup>53</sup> For a small system, the LOM for a given bulk phase may occur significantly outside the stable phase boundary of that phase, but as  $L \rightarrow \infty$ , the LOM approaches the stable phase boundary. We show an example in Fig. 2(b), where we plot the LOM for the bulk  $\mathcal{B}$  phase for  $L = 64$ . The LOM for each of our system sizes with  $L > 64$  lies between the boundary shown in Fig. 2(b) and the  $\mathcal{AB}$  and  $\mathcal{BC}$  coexistence curves. Therefore most of our results for  $n_c$  in Fig. 12 are obtained beyond the LOM of the bulk  $\mathcal{B}$  phase for the system sizes studied here, demonstrating that the FPT remains well-defined even when the bulk  $\mathcal{B}$  phase is unstable. Furthermore, small fluctuations occurring within the  $\mathcal{A}$  phase always resemble the  $\mathcal{B}$  phase, even when the bulk  $\mathcal{B}$  phase is unstable, in both the  $n_c < n^*$  and the  $n_c > n^*$  regimes. These observations emphasize that a local structure that is unstable as a bulk phase can still play a significant role, both as the dominant small fluctuation and as an “intermediate phase” in a TSN process.

## VII. RELATIONSHIP TO PREVIOUS MODELLING OF TWO-STEP NUCLEATION

As indicated in the Introduction, a number of previous simulation and theoretical studies have examined

behavior related to TSN. Previous studies have also demonstrated that many complex nucleation phenomena can be elucidated by studying lattice models similar to the one employed here.<sup>17,19,20,61–67</sup> Notably, this work reproduces several phenomena first identified by Duff and Peters<sup>17</sup> who also used a lattice model. Their work introduced the FES in the specific form that we use and showed that the conversion of the nucleus to the stable phase can occur before or after the transition state, although in the latter case the conversion of the nucleus was not explicitly observed. Their simulations also did not allow the calculation of FES of sufficient resolution to resolve the first-order character of the FPT as observed here, and they did not identify the spinodals that bracket the FPT. Reference 17 presents a CNT-based analysis of TSN, although the implications for the nature of fluctuations in general was not explored.

The analytical study of TSN by Iwamatsu<sup>21</sup> identified the thermodynamic conditions for the conversion of the nucleus to the stable phase, pointed out its first-order character, and noted that this conversion crosses a ridge in the FES. This work also showed that the FES may display two distinct saddle points, as observed here. However, Ref. 21 argued that there were cases where the FES has two independent channels leading out of the metastable phase, in contrast to our results, where we find only one. Furthermore, Ref. 21 did not identify cases in which the conversion of the nucleus to the stable phase occurs before reaching the transition state, nor did it identify spinodal endpoints along any channel in the FES. These differences may arise from fundamental differences between our modelling and that in Ref. 21. However, it is also possible that a higher resolution analysis of the cases presented in Ref. 21 might reveal the same pattern of behavior observed here. Such a test to see if Ref. 21 can be reconciled with our results merits investigation as this would clarify the possible topologies of the nucleation pathway in TSN. As mentioned earlier, our observation of spinodals bracketing the FPT is consistent with the analysis of Harrowell on the stability of sub-critical crystal nuclei,<sup>60</sup> and so it would be useful to assess the generality of this result by re-examining the features of the FES as presented in both Refs. 17 and 21.

A recent example consistent with the pattern of behavior shown here is the simulation study by Santra, Singh, and Bagchi,<sup>41</sup> which focusses on the competition between BCC and FCC crystal nucleation in a hard-core repulsive Yukawa system. They showed that a post-critical BCC nucleus forms and grows spontaneously even under conditions where bulk FCC is the most stable phase. This case corresponds to the  $n_c > n^*$  regime identified here. Reference 41 also evaluates 1D “cuts” through the FES, which in the terminology of this work correspond approximately to  $f = 0$  (BCC-like) and  $f = 1$  (FCC-like). Although the behavior of the 1D nucleation barriers so obtained is consistent with the 2D surfaces studied here, it would be useful to confirm this correspondence by computing the full 2D FES for the system studied in Ref. 41.

While several of the phenomena reported here have been documented in prior studies, these observations are fragmented across separate studies and are also limited in the

range of thermodynamic conditions examined. The general pattern of behavior presented here captures the key features of these earlier studies, clarifies the interrelationships of these findings, and also reveals important details of the FES not previously appreciated. We further show how the properties of the FES evolve over a wide range of thermodynamic conditions and correlate these changes to stable and metastable coexistence boundaries in the bulk phase diagram. Notably, no previous work has to our knowledge pointed out that the FPT is an intrinsic property of fluctuations and is distinct and independent from nucleation phenomena. Our work thus broadens, clarifies, and hopefully simplifies the conceptual framework for understanding the many phenomena associated with TSN.

### VIII. DISCUSSION

In summary, we have attempted to clarify TSN by first disentangling the physics of the FPT from the nucleation process itself and showing that these are indeed distinct phenomena. We then examine how these two phenomena combine to produce TSN via a high-resolution study of the nucleation FES for a prototypical lattice model, conducted over a wide range of thermodynamic conditions.

To highlight the correspondence between the theoretical predictions of Sec. II and the realization of these predictions in our lattice model, we present in Fig. 14 a figure analogous to Fig. 1 but where the free energy is given by  $\bar{G}(n)$  as computed

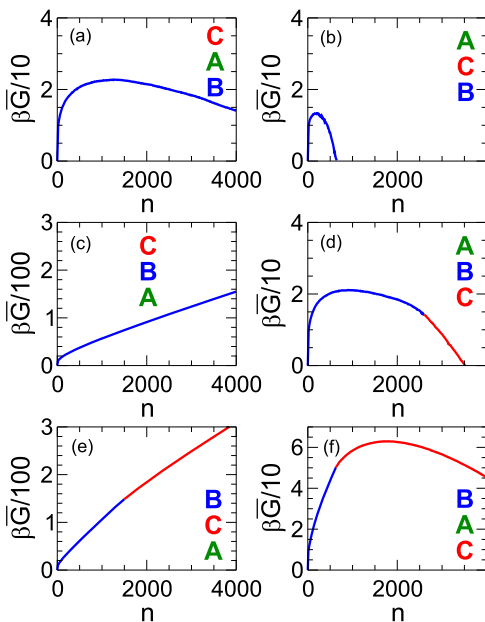


**FIG. 14.**  $\bar{G}(n)$  at the six state points identified by open circles in the upper panel of Fig. 2 and representative of the six regions of the phase diagram labelled (a)–(f). The thermodynamic properties of the phases and their interfaces at each state point are given in Table I. To indicate the relative stability of the three bulk phases at each state point, the phases are listed vertically according to their value of  $\mu$ , with  $\mu$  increasing from bottom to top in each list. In each panel,  $\bar{G}(n)$  is rendered in blue when  $n < n_c$  and in red when  $n > n_c$ .

directly from our lattice model under conditions corresponding to each of the six regimes identified in Fig. 1. The six state points (a)–(f) examined in Fig. 14 are identified by the open circles in the phase diagram shown in the upper panel of Fig. 2. The thermodynamic properties of the phases at these state points, estimated as described in Secs. S3 and S4 of the supplementary material, are given in Table I. In Fig. 14, the curve for  $\bar{G}(n)$  is blue when  $n < n_c$  (where the nucleus is dominated by  $\mathcal{B}$ ) and red when  $n > n_c$  (where the nucleus is dominated by  $\mathcal{C}$ ). In Fig. 1, the observed free energy will be either  $G_{AB}$  or  $G_{AC}$ , whichever is lower at a given  $n$ . In Fig. 14, the directly observed curve in each panel qualitatively matches the prediction from the corresponding panel in Fig. 1. The last column of Table I confirms that the condition in Eq. (3) is satisfied in all cases and, as predicted in Sec. II, we find that the nucleus starts out as a  $\mathcal{B}$  cluster at all six state points. Furthermore, in regions (d)–(f) of the phase diagram, an FPT occurs as the nucleus grows, regardless of whether the  $\mathcal{A}$  phase is stable [as in (e)] or metastable [as in (d) and (f)]. In region (d), the FPT occurs beyond the critical size, while in (f) it occurs before it.

Both our theoretical and simulation results thus demonstrate that under thermodynamic conditions commonly encountered in nucleation (e.g., near a triple point), the initial fluctuation of the system away from its equilibrium state takes the form of a local structure with the lowest surface tension with the surrounding phase. In other words, polymorph selection at the local level is under these conditions controlled by surface tension. When the lowest-surface-tension structure does not correspond to the most stable phase and Eq. (3) is satisfied, then the initial stage of nucleus growth will not resemble the stable phase and the result is TSN. The conversion of the fluctuation to the stable phase is a first-order FPT, which occurs by traversing a ridge in the FES. The transition state by which the system exits the metastable phase occurs at a saddle point in the FES and may occur before ( $n_c < n^*$ ) or after ( $n_c > n^*$ ) the FPT.

The Ostwald step rule (OSR) states that the bulk phase that forms first from a metastable phase is not the most stable phase but the phase with the chemical potential that is below but closest to the metastable phase.<sup>7,9,26,41</sup> Our findings are consistent with the OSR but also provide a modified and more general way of understanding it. In our lattice model, when metastable  $\mathcal{A}$  transforms to stable  $\mathcal{C}$ , the  $\mathcal{B}$  phase always

**TABLE I.** Chemical potential  $\mu$  of each phase and surface tension  $\sigma$  of the  $\mathcal{AB}$  and  $\mathcal{AC}$  interfaces, at each state point identified by the open circles in the upper panel of Fig. 2. These state points are representative of the six regimes of behavior labelled (a)–(f) in Figs. 1, 2, and 14. The quantity  $\delta = \phi(\sigma_{AC} - \sigma_{AB}) - \Delta\mu_{CB}$  is positive if the condition in Eq. (3) is satisfied and negative if not.

Label	H	$H_s$	$\mu_A/J$	$\mu_B/J$	$\mu_C/J$	$\sigma_{AB}/J$	$\sigma_{AC}/J$	$\delta/J$
(a)	4.01	−0.01	−0.0105	−0.0207	0.0087	0.195	0.544	1.265
(b)	4.01	0.01	0.0087	−0.0207	−0.0105	0.195	0.544	1.246
(c)	3.98	−0.02	−0.0189	0.0070	0.0195	0.195	0.662	1.667
(d)	3.98	0.02	0.0195	0.0070	−0.0189	0.195	0.662	1.628
(e)	3.92	−0.02	−0.0164	0.0625	0.0220	0.195	0.850	2.281
(f)	3.92	0.02	0.0220	0.0625	−0.0164	0.195	0.850	2.242

appears first at the local level, regardless of whether  $\mathcal{B}$  has a higher or lower chemical potential. It is the low  $\mathcal{AB}$  surface tension that ensures that  $\mathcal{B}$  forms first within  $\mathcal{A}$ ; their relative chemical potentials are initially irrelevant. When  $n_c < n^*$ , the initial sub-critical nucleus resembles the  $\mathcal{B}$  phase, but because the FPT occurs prior to the transition state, there is no indication in the post-critical nucleus that the  $\mathcal{B}$  phase was initially dominant. However, when  $n_c > n^*$ , the post-critical nucleus resembles the  $\mathcal{B}$  phase, creating the conditions in which the OSR may be realized. The OSR is formally obeyed in our model phase diagram in the region bounded by  $\mathcal{L}_{AB}$ ,  $\mathcal{L}_{BC}$ , and the LOM of the  $\mathcal{B}$  phase (region “O<sub>1</sub>” in Fig. 2) because this is the region in which  $\mathcal{B}$  is both observable as a bulk metastable phase and also has a lower chemical potential than  $\mathcal{A}$ . At points in the phase diagram between  $\mathcal{L}_{AB}$  and  $\mathcal{L}_{BC}$  but beyond the LOM of the  $\mathcal{B}$  phase (region “O<sub>2</sub>” in Fig. 2), the bulk  $\mathcal{B}$  phase is unstable. In this region, the post-critical nucleus will resemble  $\mathcal{B}$  but must convert to the stable  $\mathcal{C}$  phase at a finite size that is smaller than the system size. Thus the observation of behavior that obeys the OSR depends on an interplay of system-size effects (which control the location of the LOM) and the range of  $n_{\max}$  for the growing post-critical nucleus over which the low- $f$  channel in the FES remains well-defined (which is controlled by the location of the spinodal on the low- $f$  channel). In this study, we have restricted our evaluation of the FES to the range of  $n_{\max}$  in which the largest fluctuation does not approach the system size. It would be useful for future work to extend the FES to larger  $n_{\max}$  to further clarify the behavior related to the OSR.

As noted, the two steps in TSN are qualitatively different. One crosses a saddle point in the FES, and the other crosses a ridge. As such, both steps are activated processes. At the same time, the process that takes the system over the saddle point is similar to that in conventional (i.e., one-step) nucleation, while the ridge-crossing process of the FPT is more complex. The FPT occurs in a system (the fluctuation) the size of which is spontaneously increasing or decreasing, depending on the shape of the FES. Furthermore, there is a well-defined critical size for the nucleus of the stable phase to form inside the fluctuation, and until the fluctuation itself reaches this size, the stable phase will not be observed. This interplay of size effects is consistent with the existence of the spinodal limit of the high- $f$  channel on the FES that prevents a  $\mathcal{C}$ -like fluctuation from being stable at small  $n_{\max}$  and suggests that this phenomenon is indeed general.<sup>60</sup> In addition, the existence of a spinodal limit at large  $n_{\max}$  along the low- $f$  channel means that if the growing  $\mathcal{B}$  nucleus does not cross the ridge to the  $\mathcal{C}$  phase, then it will ultimately do so via a barrierless process at the spinodal. That is, the activated nature of the ridge-crossing FPT process is lost if the  $\mathcal{B}$  nucleus grows sufficiently large.

We also emphasize that this work explicitly considers only the thermodynamic aspects of TSN and that our conclusions apply to a system in which all degrees of freedom are sampled in equilibrium. We have not modelled kinetic effects, which are well known to play an important role in phase transitions generally. For example, in a bulk phase transition from a supercooled liquid to a crystal, sluggish kinetics may

completely prevent the formation of the thermodynamically-favored crystal phase on laboratory time scales, resulting in glass formation. Similarly, if the relaxation time for variations in  $f$  near a FPT greatly exceed the time scale for changes in the size of a fluctuation, the FPT may never be observed. In the case of our lattice model when  $n_c > n^*$  [e.g., Fig. 8(c)], this effect would cause the system to be kinetically trapped in the low- $f$  channel of the FES, resulting in the formation of the metastable  $\mathcal{B}$  phase, despite the greater thermodynamic stability of the  $\mathcal{C}$  phase. Previous simulation studies have demonstrated the existence of such kinetic effects during nucleation. For example, Ref. 68 presents the case of a binary mixture of charged colloids where the nucleation of a charge-disordered fcc bulk phase is observed under conditions where a charge-ordered bcc phase is both more stable and has a lower nucleation barrier. In this case, the relaxation of the local structure from disordered-fcc to ordered-bcc is too slow to occur on the time scale of nucleation, preventing the observation of the bcc phase. In a simulation study of diamond nucleation,<sup>69</sup> conditions were identified where the initial fluctuations of the melt were found to be similar to those of graphite rather than the more-stable diamond phase. This effect was attributed to the lower surface tension of the graphite-melt interface, compared to the diamond-melt interface, an observation in line with the predictions of this work. Furthermore, small graphite-like fluctuations were never observed to convert to the diamond structure, perhaps, because the kinetics for this process is too slow or perhaps because the most stable bulk structure (diamond) is thermodynamically unstable as a small fluctuation, as suggested by our lattice model results. These examples demonstrate both that dramatic kinetics effects are to be expected in TSN and also that a clearer understanding of the thermodynamic landscape underlying the nucleation process is critical for interpreting these kinetics effects.

We note further that all of our analysis concerning TSN assumes that the intermediate phase ( $\mathcal{B}$ ) completely wets the stable phase ( $\mathcal{A}$ ), a condition realized in our lattice model. An important direction for future work is to generalize these considerations to cases in which incomplete wetting occurs. In addition, the lattice model results presented here are all obtained at fixed  $T$ . While this constraint has simplified our analysis, now that the characteristics of the model FES have been described in detail, it will be interesting in subsequent studies to explore the  $T$  dependence of these features, especially for the FPT itself.

Our work also has a number of practical implications for simulation studies of nucleation. It is widely appreciated that care must be taken when choosing a local order parameter to define the nucleus, the size of which serves as the reaction coordinate in many studies which evaluate the nucleation barrier.<sup>57,58,70,71</sup> Our results show that when this order parameter recognizes both the intermediate and the stable phase contributions to the nucleus, the “kink” in  $G_1$  is a characteristic signature of TSN, which also locates  $n_c$ . Such a kink may be discerned in previous studies; see, e.g., Fig. 2 of Ref. 32. Conversely, caution must be exercised when conducting 1D umbrella sampling with respect to  $n_{\max}$ : If  $n_c$  is large, then

the barrier between the low- $f$  and high- $f$  channels will also be large, and so a series of simulations of progressively larger  $n_{\max}$  may become trapped in the low- $f$  channel even when  $n_{\max} > n_c$ . When practical, 2D umbrella sampling to compute the full FES should be carried out, to ensure that the complete nucleation pathway is observed. It is also common to choose a local order parameter which only detects a nucleus of the stable phase. Our work demonstrates that when TSN occurs, the initial nuclei generated by this approach will not correspond to the most probable initial nuclei, resulting in a distortion in the shape of  $G_1$  at small  $n$ . Where possible, a local order parameter should be chosen that identifies all structures that deviate from the metastable phase, not just those that resemble the stable phase. Recent work suggests that such an approach is feasible in molecular systems.<sup>72</sup> Finally, we note the challenges that will be associated with estimating the nucleation rate from transition state theory when the transition state is not sharply defined in the FES, as in Fig. 8(b).<sup>58</sup> This difficulty may help explain the large deviations between estimated and observed nucleation rates noted for many systems exhibiting complex nucleation processes.<sup>7,23</sup>

In addition, it is notable that in our lattice model we observe conditions where the most probable fluctuation of a given size does not correspond to a stable bulk phase under the same conditions, i.e., conditions beyond the LOM of the bulk phase. Sear noted a similar effect in a simulation study of heterogeneous nucleation.<sup>66</sup> It is therefore conceivable that, in other systems, a local fluctuation that never corresponds to a bulk phase might play an important role in the growth of the nucleus. Such fluctuations might include amorphous solid clusters or spatially limited structures such as icosahedra.<sup>3</sup> This possibility, combined with the activated nature of the FPT, could account for long-lived metastable “prenucleation clusters” that grow to mesoscopic size before conversion to the stable phase, as has been reported, e.g., in crystallization of  $\text{CaCO}_3$ .<sup>15,16,22,27</sup>

We have shown that the dominant contribution of the surface tension to the free energy of small fluctuations underlies and explains the complexities of TSN observed near the triple point of our model system. Recent work on the competition between glass and crystal formation in supercooled liquids also points to the central role of low-surface-tension fluctuations,<sup>73</sup> which if different from the stable crystal can promote glass formation. The controlling influence of the surface tension in determining the most probable initial deviation from equilibrium may therefore be a principle with wide ranging implications for the behavior of metastable systems.

## SUPPLEMENTARY MATERIAL

See [supplementary material](#) for a description of the details of our simulation methods and for additional plots of the free energy surface  $G(n_{\max}, f)$ .

## ACKNOWLEDGMENTS

I.S.-V., R.K.B., and P.H.P. thank NSERC for support. P.H.P. also acknowledges the support from the Dr. W. F. James

Research Chair Program. Computational resources were provided by ACEnet and Compute Canada. We thank K. DeBell, D. Eaton, K. M. Poduska, F. Sciortino, and R. Timmons for helpful discussions.

## REFERENCES

- 1 H. E. Stanley, *Introduction to Phase Transitions and Critical Phenomena* (Oxford University Press, Oxford, 1971).
- 2 L. Berthier and G. Biroli, *Rev. Mod. Phys.* **83**, 587 (2011).
- 3 C. P. Royall and S. R. Williams, *Phys. Rep.* **560**, 1 (2015).
- 4 F. Turci, C. P. Royall, and T. Speck, *Phys. Rev. X* **7**, 031028 (2017).
- 5 M. A. Anisimov, M. Duška, F. Caupin, L. E. Amrhein, A. Rosenbaum, and R. J. Sadus, *Phys. Rev. X* **8**, 011004 (2018).
- 6 P. G. Debenedetti, *Metastable Liquids. Concepts and Principles* (Princeton University Press, Princeton, New Jersey, 1996).
- 7 K. F. Kelton and A. L. Greer, *Nucleation in Condensed Matter. Applications in Materials and Biology* (Elsevier, Oxford, 2010).
- 8 P. R. ten Wolde and D. Frenkel, *Science* **277**, 1975 (1997).
- 9 Z. Tavassoli and R. P. Sear, *J. Chem. Phys.* **116**, 5066 (2002).
- 10 P. G. Vekilov, *Cryst. Growth Des.* **4**, 671 (2004).
- 11 W. Pan, A. B. Kolomeisky, and P. G. Vekilov, *J. Chem. Phys.* **122**, 174905 (2005).
- 12 J. F. Lutsko and G. Nocolis, *Phys. Rev. Lett.* **96**, 046102 (2006).
- 13 J. A. van Meel, A. J. Page, R. P. Sear, and D. Frenkel, *J. Chem. Phys.* **129**, 204505 (2008).
- 14 B. Chen, H. Kim, S. J. Keasler, and R. B. Nellas, *J. Phys. Chem. B* **112**, 4067 (2008).
- 15 D. Gebauer, A. Völkel, and H. Cölfen, *Science* **322**, 1819 (2008).
- 16 E. M. Pouget, P. H. H. Bomans, J. A. C. M. Goos, P. M. Frederik, G. de With, and N. A. J. M. Sommerdijk, *Science* **323**, 1455 (2009).
- 17 N. Duff and B. Peters, *J. Chem. Phys.* **131**, 184101 (2009).
- 18 P. G. Vekilov, *Nanoscale* **2**, 2346 (2010).
- 19 S. Whitelam, *J. Chem. Phys.* **132**, 194901 (2010).
- 20 L. O. Hedges and S. Whitelam, *J. Chem. Phys.* **135**, 164902 (2011).
- 21 M. Iwamatsu, *J. Chem. Phys.* **134**, 164508 (2011).
- 22 R. Demichelis, P. Raiteri, D. Quigley, D. Gebauer, and J. D. Gale, *Nat. Commun.* **2**, 590 (2011).
- 23 R. P. Sear, *Int. Mater. Rev.* **57**, 328 (2012).
- 24 M. Iwamatsu, *Phys. Rev. E* **86**, 041604 (2012).
- 25 M. Iwamatsu, *J. Chem. Phys.* **136**, 044701 (2012).
- 26 M. Santra, R. S. Singh, and B. Bagchi, *J. Phys. Chem. B* **117**, 13154 (2013).
- 27 A. F. Wallace, L. O. Hedges, A. Fernandez-Martinez, P. Raiteri, J. D. Gale, G. A. Waychunas, S. Whitelam, J. F. Banfield, and J. J. De Yoreo, *Science* **341**, 885 (2013).
- 28 Y. Peng, F. Wang, Z. Wang, A. M. Alsayed, Z. Zhang, A. G. Yodh, and Y. Han, *Nat. Mater.* **14**, 101 (2014).
- 29 M. Salvalaglio, C. Perego, F. Giberti, M. Mazzotti, and M. Parrinello, *Proc. Natl. Acad. Sci. U. S. A.* **112**, E6 (2015).
- 30 K. Kratzer and A. Arnold, *Soft Matter* **11**, 2174 (2015).
- 31 S. M. A. Malek, G. P. Morrow, and I. Saika-Voivod, *J. Chem. Phys.* **142**, 124506 (2015).
- 32 W. Qi, Y. Peng, Y. Han, R. K. Bowles, and M. Dijkstra, *Phys. Rev. Lett.* **115**, 185701 (2015).
- 33 G. C. Sosso, J. Chen, S. J. Cox, M. Fitzner, P. Pedevilla, A. Zen, and A. Michaelides, *Chem. Rev.* **116**, 7078 (2016).
- 34 S. Ishizuka, Y. Kimura, T. Yamazaki, T. Hama, N. Watanabe, and A. Kouchi, *Chem. Mater.* **28**, 8732 (2016).
- 35 C. Guo, J. Wang, J. Li, Z. Wang, and S. Tang, *J. Phys. Chem. Lett.* **7**, 5008 (2016).
- 36 Y. Bi, A. Porras, and T. Li, *J. Chem. Phys.* **145**, 211909 (2016).
- 37 M. Iwamatsu, *Phys. Rev. E* **95**, 042803 (2017).
- 38 C.-T. Lee and E. M. Terentjev, *J. Chem. Phys.* **147**, 105103 (2017).

- <sup>39</sup>F. Zhang, *J. Phys.: Condens. Matter* **29**, 443002 (2017).
- <sup>40</sup>T. Yamazaki, Y. Kimura, P. G. Vekilov, E. Furukawa, M. Shirai, H. Matsumoto, A. E. S. Van Driessche, and K. Tsukamoto, *Proc. Natl. Acad. Sci. U. S. A.* **114**, 2154 (2017).
- <sup>41</sup>M. Santra, R. S. Singh, and B. Bagchi, *Phys. Rev. E* **98**, 032606 (2018).
- <sup>42</sup>A. E. S. Van Driessche, N. Van Gerven, P. H. H. Bomans, R. R. M. Joosten, H. Friedrich, D. Gil-Carton, N. A. J. M. Sommerdijk, and M. Sleutel, *Nature* **556**, 89 (2018).
- <sup>43</sup>K. Binder and D. Landau, *A Guide to Monte Carlo Simulations in Statistical Physics*, 3rd ed. (Cambridge University Press, New York, 2009).
- <sup>44</sup>D. P. Landau, *Phys. Rev. Lett.* **28**, 449 (1972).
- <sup>45</sup>D. P. Landau and R. H. Swendsen, *Phys. Rev. Lett.* **46**, 1437 (1981).
- <sup>46</sup>P. A. Rikvold, W. Kinzel, J. D. Gunton, and K. Kaski, *Phys. Rev. B* **28**, 2686 (1983).
- <sup>47</sup>H. J. Herrmann, *Phys. Lett. A* **100**, 256 (1984).
- <sup>48</sup>D. P. Landau and R. H. Swendsen, *Phys. Rev. B* **33**, 7700 (1986).
- <sup>49</sup>C. Borgs and R. Kotecký, *J. Stat. Phys.* **61**, 79 (1990).
- <sup>50</sup>K. Binder, *Eur. Phys. J. B* **64**, 307 (2008).
- <sup>51</sup>M. E. Tuckerman, *Statistical Mechanics: Theory and Molecular Simulation* (Oxford University Press, Oxford, 2010).
- <sup>52</sup>K. Binder, B. Block, S. K. Das, P. Virnau, and D. Winter, *J. Stat. Phys.* **144**, 690 (2011).
- <sup>53</sup>K. Binder, B. J. Block, P. Virnau, and A. Tröster, *Am. J. Phys.* **80**, 1099 (2012).
- <sup>54</sup>S. Ryu and W. Cai, *Phys. Rev. E* **81**, 030601 (2010).
- <sup>55</sup>S. Kumar, D. Bouzida, R. H. Swendsen, P. A. Kollman, and J. M. Rosenberg, *J. Comput. Chem.* **13**, 1011 (1992).
- <sup>56</sup>A. Grossfield, WHAM: The Weighted Histogram Analysis Method, Version 2.0.9, 2018, <http://membrane.urmc.rochester.edu/content/wham>.
- <sup>57</sup>P. R. ten Wolde, M. J. Ruiz-Montero, and D. Frenkel, *Faraday Discuss.* **104**, 93 (1996).
- <sup>58</sup>S. Auer and D. Frenkel, *J. Chem. Phys.* **120**, 3015 (2004).
- <sup>59</sup>S. E. M. Lundrigan and I. Saika-Voivod, *J. Chem. Phys.* **131**, 104503 (2009).
- <sup>60</sup>P. Harrowell, *J. Phys.: Condens. Matter* **22**, 364106 (2010).
- <sup>61</sup>R. Sear, *J. Phys.: Condens. Matter* **17**, 3997 (2005).
- <sup>62</sup>A. J. Page and R. P. Sear, *Phys. Rev. Lett.* **97**, 065701 (2006).
- <sup>63</sup>R. P. Sear, *J. Phys.: Condens. Matter* **19**, 466106 (2007).
- <sup>64</sup>R. P. Sear, *J. Chem. Phys.* **129**, 164510 (2008).
- <sup>65</sup>R. P. Sear, *Europhys. Lett.* **83**, 66002 (2008).
- <sup>66</sup>R. P. Sear, *J. Chem. Phys.* **131**, 074702 (2009).
- <sup>67</sup>R. P. Sear, *J. Phys.: Condens. Matter* **24**, 052205 (2011).
- <sup>68</sup>E. Sanz, C. Valeriani, D. Frenkel, and M. Dijkstra, *Phys. Rev. Lett.* **99**, 055501 (2007).
- <sup>69</sup>L. Ghiringhelli, C. Valeriani, E. Meijer, and D. Frenkel, *Phys. Rev. Lett.* **99**, 055702 (2007).
- <sup>70</sup>L. C. Jacobson, M. Matsumoto, and V. Molinero, *J. Chem. Phys.* **135**, 074501 (2011).
- <sup>71</sup>A. Reinhardt, J. P. K. Doye, E. G. Noya, and C. Vega, *J. Chem. Phys.* **137**, 194504 (2012).
- <sup>72</sup>Z. Krebs, A. B. Roitman, L. M. Nowack, C. Liepold, B. Lin, and S. A. Rice, *J. Chem. Phys.* **149**, 034503 (2018).
- <sup>73</sup>J. Russo, F. Romano, and H. Tanaka, *Phys. Rev. X* **8**, 021040 (2018).